Estimates of plume height from infrasound for regional volcano monitoring

Anna Perttu [a,*], Benoit Taisne [a,b], Silvio De Angelis [c], Jelle D. Assink [d], Dorianne Tailpied [a], Ross Adrian Williams [e]

[a] Earth Observatory of Singapore, Nanyang Technological University, 50 Nanyang Ave, 639798, Singapore
[b] Asian School of the Environment, Nanyang Technological University, 50 Nanyang Ave, 639798, Singapore
[c] School of Environmental Sciences, University of Liverpool, Liverpool L69 3GP, United Kingdom
[d] R&D Seismology and Acoustics, Royal Netherlands Meteorological Institute (KNMI), P.O. Box 201, 3730 AE De Bilt, the Netherlands
[e] School of Art, Design and Media, Nanyang Technological University, 50 Nanyang Avenue, 639798, Singapore

ARTICLE INFO

ABSTRACT

Present efforts in volcano monitoring, particularly in Southeast Asia, rely on the combination of local data (generally gathered at less than 100 km from the volcano), and satellite remote sensing. While this combination has its strengths, there are still weaknesses that the use of ground-based remote sensing data - such as distant infrasound measurements - could help alleviate. Infrasound offers tools for detecting and characterizing volcanic plumes independent of cloud cover and time of day. Larger volcanic eruptions generate infrasound that is related to the plume and offers a unique view into eruption dynamics within the context of monitoring. Past research has demonstrated that infrasound can be used to estimate source parameters, such as the rate at which material is ejected from volcanic vents during eruptions; these are key input parameters into empirical and numerical models to estimate the height of volcanic plumes, atmospheric ash transport and dispersion. Here, we demonstrate the use of remote infrasound in estimating the height of volcanic plumes, including a case study on the May 30, 2014 plume from the volcano Sangeang Api in Indonesia. We were able to determine the plume height using infrasound gathered from 2000 to over 5000 km distance from the volcano. During the January 2020 eruption of Taal volcano in the Philippines, this method was applied to remote infrasound recorded 1650 km to the east. We show that our workflow can be implemented in near real-time, offering an effective tool for rapid plume height measurement, including associated uncertainties, when volcanic clouds are not visible from the ground or space.

1. Introduction

Volcanoes are traditionally monitored using a combination of local ground-based sensors and satellite remote sensing. Both methods have inherent drawbacks: local monitoring networks are vulnerable during large volcanic eruptions, and satellite remote sensing is dependent on observational conditions, satellite coverage, and types of instruments available for observation. Even the Himawari-8 satellite in Southeast Asia finds plumes below the cloud cover layer very difficult to detect. It is a geostationary weather satellite operated by the Japanese Meteorological Agency and has optical sensors in both the visible and infrared bands (Bessho et al., 2016) and a 10-minute repeat time. There are around 750 active or potentially active volcanoes within Southeast (SE) Asia, and the decade probability of a large (VEI 4+) eruption in the region is nearly 100% (Whelley et al., 2015). In addition to local hazards derived from such eruptions, in recent decades air

traffic in the region has drastically increased; seat capacity has nearly tripled between 1998 and 2013 (Bowen, 2016) and is expected to triple again in the 2030s (Aneeka and Zhong, 2016). Encounters between aircraft and volcanic ash are known to result in significant damage to airplanes even causing loss of power to their engines (Guffanti et al., 2010; Lechner et al., 2018). Therefore, timely delivery of alerts of ongoing eruptive activity to the aviation industry is essential. These require identification of an eruption in time and space and rapid estimates of parameters such as the maximum height of volcanic plumes, a key input into models to produce forecasts of atmospheric ash dispersal. Infrasound offers a cloud cover independent technology capable of not only detection, but also characterization of volcanic activity on a regional to global scale.

Infrasound has become a well-established research method to estimate the source parameters of volcanic eruptions using data recorded at the local scale, that is within 100 km from the active vent (Vergniolle and Caplan-Auerbach, 2006; Caplan-Auerbach et al., 2010; Ripepe et al., 2013; Johnson and Miller, 2014; Kim et al., 2015; Lamb et al., 2015; Yamada et al., 2017; De Angelis et al., 2019). Early work

* Corresponding author.
 E-mail address: aperttu@ntu.edu.sg (A. Perttu).

assumed that at this range attenuation of the acoustic signal is dominated by geometric spreading; more recent studies demonstrated that topographic effects that can have significant impact on signal attenuation (Kim and Lees, 2011; Lacanna and Ripepe, 2013a; Kim et al., 2015; Diaz-Moreno et al., 2019; Iezzi et al., 2019). However, detailed calculations of the effect of atmospheric conditions on the propagation of the acoustic wavefield are not always considered (Caplan-Auerbach et al., 2010; Fee et al., 2010; Lamb et al., 2015). While local infrasound sensors are not always installed, data are frequently available from a number of regional networks worldwide, which have been used for volcano monitoring in the past (Dabrowa et al., 2011; Matoza et al., 2011; Matoza et al., 2017, 2019). In this paper *local* infrasound stations refers to instruments at distances up to 100 km from a volcano, *regional-to-global* indicates sensors at larger distances.

The International Monitoring System (IMS) is a global network which is in place for the verification of the Comprehensive Nuclear-Test-Ban Treaty (CTBT) and consists of seismic, hydro-acoustic and infrasound stations as well as radionuclide detectors. The infrasound component of the network allows for regional- to global-scale monitoring of volcanoes (Dabrowa et al., 2011; Matoza et al., 2011, 2017, 2019; Tailpied et al., 2013). There are several challenges for timely detection and characterization of signals with regional infrasound. These include station availability within range, data quality of available stations, modeling of the attenuation between the sensor and the source, which all have an impact on the ability to reconstruct the signal and its amplitude at the source.

Due to advances in infrasound propagation modeling, it now is possible to estimate the source amplitude of a volcanic infrasound signal at long range, with associated uncertainties, using full-wave propagation modeling methods such as Parabolic Equation (PE) techniques. More information on atmospheric infrasound propagation modeling and the state-of-the-art of propagation algorithms can be found in the review papers by Norris et al., 2010 and Waxler and Assink (2019). As detailed propagation computations can be time consuming and require specific expertise, approximate methods can fulfill a role for near real-time applications for which timeliness is a crucial factor. Le Pichon et al. (2012) developed a frequency-dependent attenuation relation by fitting a functional form to the transmission loss computed using a PE model for an ensemble of candidate atmospheres. The resulting attenuation relationship approximates full-wave propagation effects, including geometric spreading and intrinsic absorption, and uses realistic atmospheric specifications and source effects. This method, referred to as *atmospheric attenuation modeling*, has been applied to the optimization of networks for monitoring of volcanoes by regional infrasound (Tailpied et al., 2017).

In this study, we explore the feasibility of applying methods that have been established using local infrasound for volcanic eruption source parameter estimation at the regional-to-global (>100 km) scale. In addition, the errors associated with the method will be examined, allowing for a realistic uncertainty in the calculations. Source parameter calculations, and specifically those for estimating plume height, have been an area of active research within the volcano infrasound community, with the most recent developments focusing on waveform inversions (De Angelis et al., 2019). However, the network requirements for performing a well-defined inversion include multiple infrasound sensors circling the volcano, and this is not always available or practical. The common configurations for local infrasound installations are single sensors, either on their own or co-located with other equipment, or an array configuration at one or more locations. Additionally, not all infrasound sensors installed at volcanoes are telemetered or used in monitoring.

The method presented in this paper is applied to a case study of the May 30th, 2014, eruption of the volcano Sangeang Api in Indonesia. The eruption produced unambiguous infrasound detections throughout the region and was clearly observed both from the ground and with satellite imagery, providing ground truthing data (Global Volcanism Program, 2014b; Zidikheri et al., 2017). This paper examines the potential for infrasound to estimate source parameters like plume height and exit velocity for large eruptions at a regional scale. It combines established methods for use at a local scale (Vergniolle and Caplan-Auerbach, 2006; Caplan-Auerbach et al., 2010; Lamb et al., 2015), with atmospheric attenuation modeling (Le Pichon et al., 2012, 2019; Tailpied et al., 2017). In order to illustrate the potential of the method for expediting alerts in the region, this study also compares the timing of infrasound arrivals (and associated plume height estimations) with the timing of the Volcano Ash Advisory Center (VAAC) alerts (http://www.bom.gov.au/aviation/volcanic-ash/). While, in this example, clear satellite observations were available, there is not one technology that will effectively monitor all volcanoes in all circumstances. However, by combining different technologies, the overall detection capability can be improved.

2. Methodology

Previous work on estimating both exit velocity and plume height from infrasound has focused on signals recorded locally (<100 km), at a range where attenuation is dominated by geometric spreading and topography, and therefore more complex attenuation models are not required. This section presents our proposed novel approach to relate acoustic power and acoustic radiation patterns to exit velocity at the vent from remote infrasound building on standard methods developed in past studies. First, the variations in the calculation of acoustic power are discussed for the established local case. Modifications are introduced in order to expand the area over which this method can be applied to the regional case. We have also highlighted areas where errors may be introduced due to uncertainties for different values and parameters within the equations. Second, the relationships between radiation pattern and exit velocity are discussed for both the local and regional cases. Finally, we examine how this can be used to estimate plume height. The methods have been presented in a step-by-step manner for ease of implementation in an operational or monitoring context.

2.1. Acoustic power

There is a long history of using acoustic power as a measure of infrasound from volcanoes (Woulff and McGetchin, 1976; Fee et al., 2010; Fee and Matoza, 2013), and employing those data to estimate source parameters (e.g. exit velocity, eruptive flux) with variations in the methodology (Vergniolle and Caplan-Auerbach, 2006; Ripepe et al., 2013; Johnson and Miller, 2014; Yamada et al., 2018; De Angelis et al., 2019). For this project, we will build on the methods presented in Caplan-Auerbach et al. (2010) and convert infrasound data recorded at remote infrasound arrays to plume height, through the calculation of acoustic power and exit velocity at the vent. Variables and units are detailed in Table 1.

Infrasound data are recorded in units of pascal (Pa), and are converted into acoustic power (Π_a) in units of Watt (W) at the source (vent) through Eq. (1),

$$\Pi_a = \Omega \frac{1}{\rho_0 c} \Delta P^2 \qquad (1)$$

where ΔP is the overpressure term, ρ_0 is the background density of air, and c is the speed of sound in air. The attenuation term, Ω, is expressed as $\gamma \pi r^2$, where γ refers to a geometric spreading constant related to the choice of surface over which the acoustic power is integrated, and r is the radiation distance (in this case the source to sensor distance). This is only valid for near-source ranges, where the atmosphere is assumed to be a homogeneous medium, and that the acoustic signal propagates in a straight line from source to receiver. Simple geometries such as topography can introduce some degree of error (Lacanna and Ripepe, 2013b). For a spherical spreading model or a hemisphere with a

Table 1

All variables used within the methodology are listed along with their units, and if known, range of values. Also included is a description of each variable.

Variable symbol	Value(s) and units	Description
γ	1, 2, 4 constant	Geometric spreading constant
Ω	m^2	Attenuation factor in the acoustic power equation
ρ	$1\ kg/m^3$	Density of air
c	$340\ m/sec$	Speed of sound in air
r	Calculated from station to volcano locations in meters	Radius of the attenuation sphere, usually the vent to sensor distance in meters
τ	$sec.$	Time window for processing (waveforms)
F_s	20 Hz (for IMS data)	Sample rate of the data
n	$n = \tau * F_s$	Number of samples
A_{ref}	$20 \times 10^{-6}\ Pa$	Reference atmospheric sound pressure
K	K_m: 1/16 (circular flat orifice) to 1 (spherical source) K_d: 10^{-2} to 10^{-1} K_q: 3×10^{-5} to 10^{-4}	Empirical constant for a monopole, dipole or quadrapole radiation
R	30 m (Sangeang Api)	Vent radius (m)
v	m/sec	Exit velocity (m/s)
Q	m^3/sec	Volumetric flux (m^3/sec)
Π	W	Acoustic power (W)
V	m^3	Cumulative volume (m^3)
m	4,6,8	Constant for generalizing radiation equations (Matoza et al., 2013)
N	Hz	Brunt-Väisälä frequency, or buoyancy frequency
Amp_{data}	dB of pressure relative to A_{ref}	Calculated amplitude of infrasound in dB for the frequency band of interest
Att_{calc}	dB of pressure	Calculated attenuation (signal loss) between source and sensor for frequency band of interest

reflection, $\gamma=4$ (Fee et al., 2010; Fee and Matoza, 2013), for hemispherical spreading, $\gamma=2$ (Dabrowa et al., 2011; Johnson and Ripepe, 2011; Jolly et al., 2016), and for a disc $\gamma=1$ (Vergniolle and Caplan-Auerbach, 2006; Caplan-Auerbach et al., 2010; Lamb et al., 2015; De Angelis et al., 2019). In general, when geometric spreading is the only attenuation considered, the preferred value for γ is 1, especially for regional-to-global range calculations. However, it is more complicated within a local range. For example, Fee et al. (2010) invoked the geometry of a volcanic system in their discussion on the radiation pattern, and argued that a reflection needs to be taken into account, leading to the use of $\gamma=4$. Note that this involves some prior knowledge of the configuration of the vent geometry and the depth of the explosions. Due to the lack of consensus on the discrete value of γ (i.e. 1, 2 or 4), it has been treated as a variable, and while the value of 1 is preferred, other values have been considered within the calculated uncertainties.

2.1.1. Local infrasound

The overpressure, ΔP, is derived from the infrasound data, and is handled differently depending on the location of the sensor relative to the source. The established methods for computing ΔP at a local range also demonstrate some variation in notation within the literature, but in practice the calculation methods are consistent. Following Vergniolle and Caplan-Auerbach (2006), we define ΔP_L, as the overpressure term on a local scale, through Eq. (2), which is also used explicitly in Caplan-Auerbach et al. (2010) and Lamb et al. (2015):

$$\Delta P_L(t_i)^2 = \frac{1}{\tau} \int_{t_i-\tau}^{t_i} |p(t_i) - p_{air}|^2 dt \qquad (2)$$

where τ is the time window over which the calculation is performed (in seconds), and $|p(t_i) - p_{air}|$ is the measured excess pressure. The overpressure term is derived from the infrasound data vector, which has been

bandpass filtered into the desired frequency band. In order to deal with discrete digitized data the integral can be approximated with the trapezoidal approximation. Thus, the vector $p(t_i)$ becomes $p(t_j)$, and Eq. (2) becomes:

$$\Delta P_L(t_i)^2 = \frac{1}{n} \sum_{j=i-n+1}^{n} \frac{|p(t_{j-1})|^2 - |p(t_j)|^2}{2} \delta t \qquad (3)$$

where $n = \tau \times F_s$, or the number of points within the time window τ, with data sample rate F_s. This method is used when working with local data and usually designed for a specific volcano.

2.1.2. Regional infrasound

For infrasound recorded at a regional-to-global range, the effect of attenuation from propagation through the atmosphere must be taken into account (Waxler and Assink, 2019). Infrasound propagates through the atmosphere via multiple refractions, with the possibility of ducting when the acoustic waves are trapped in a specific waveguide due to favorable wind conditions and temperature gradients. Such features allow for long distance propagation with relatively low attenuation (de Groot-Hedlin et al., 2009; Mutschlecner and Whitaker, 2010). Throughout the atmosphere tropospheric, stratospheric, and thermospheric waveguides can be distinguished. The stratospheric waveguide is most efficient for long-range ducting due to its persistent nature and large spatial extent. These waveguides can sustain infrasound propagation over thousands of kilometers. Conversely, the presence of a troposheric waveguide is typically more limited to moderate latitudes during winter. These waveguides exist due to a strong jet stream, which is a more fickle feature and strongly modulated by planetary waves. The thermospheric waveguide is always present but is less likely to sustain propagation over long distances. This is due to the higher degree of thermo-viscous absorption in the upper atmosphere which scales quadratically with acoustic frequency (Sutherland and Bass, 2004; Waxler and Assink, 2019).

Eqs. (2) and (3) can be used at local distances of up to about 100 km. In this range the dominant signal loss mechanism is geometric spreading, leading to amplitudes decreasing with distance as $1/r$. However, topography can have a large impact on infrasound amplitudes and may lead to deviations from this typical spreading pattern at local distances (Lacanna et al., 2014). Beyond 100 km, an acoustic "geometric shadow zone" is expected up to a distance of 200 km due to the bending of acoustic waves when they propagate through the atmosphere and a lack of expected direct arrivals (Whitaker and Norris, 2008; Evers and Haak, 2010). At distances greater than the shadow zone atmospheric modeling is required to account for the more complicated propagation through the atmosphere (Le Pichon et al., 2012).

There are different approaches to calculating the attenuation, or transmission loss along the path for infrasound. The attenuation of infrasound as it propagates through the atmosphere is due to a combination of geometric spreading as well as thermo-viscous, vibrational, and relaxational absorption mechanisms. The absorption mechanisms are frequency dependent. The approach used in this paper was initially developed by Le Pichon et al. (2012) and Tailpied et al. (2013), and is based on a semi-empirical attenuation relationship. This method takes the refractive properties of the stratospheric and thermospheric waveguides into account, including its absorption mechanisms, but does not consider the effect of tropospheric waveguides. Recent advances include the incorporation of longitudinal variations of wind and temperature profiles along the propagation path, and the effect of atmospheric uncertainties inherent in data and model (de Groot-Hedlin and Hedlin, 2014; de Groot-Hedlin, 2016; Tailpied et al., 2017; Le Pichon et al., 2019). This approach (combining the methods described in Le Pichon et al. (2012), Tailpied et al. (2017), and Le Pichon et al. (2019)) was chosen due to its computational efficiency as it is a semi-empirical transfer function and thus less time consuming. Other options include PE

techniques (Lingevitch et al., 1999; Edelmann et al., 2005), ray theory (Pilger et al., 2013), normal modes (Godin and Naugolnykh, 2005; Assink et al., 2017; Waxler et al., 2017) and finite-difference methods (de Groot-Hedlin et al., 2011; Kim and Lees, 2011).

In order to incorporate the long-range atmospheric attenuation modeling, single frequency band calculations are required, as the method used is frequency dependent. We have therefore modified Eqs. (2) and (3), and used them to calculate the ΔP term. It is common for attenuation to be reported in terms of sound pressure level (SPL), and expressed in the unit decibels (dB), also chosen for this calculation (Garces, 2013).

First, the frequency band with the highest energy within the signal of interest is selected. Dispersion will cause the signal to be spread out in the time dimension but does not generally impact the energy within a specific frequency band (Lacanna et al., 2014). Because calculations are performed over one frequency band, the selection of the band is important; the frequency with the highest energy will vary for different eruptions and can also vary between detecting stations. For this specific project, we use the INFrasonic EneRgy Nth Octave (INFERNO) method based on ANSI and ISO standard nth octave frequency bands extended into the infrasound range to determine the frequency band with the highest energy (Garces, 2013). Second, a Fast Fourier Transform (FFT) is used to calculate the amplitude (in dB) within this frequency band over the eruption signal. The conversion to dB requires a reference amplitude that should be used throughout all calculations. The signal amplitude (Amp_{data}) can be represented as either the maximum amplitude (dB) within the signal or as a vector time series of amplitude, we have chosen to use the maximum amplitude within the signal time window.

The atmospheric attenuation factor (Att_{calc}), is defined as the attenuation from the reduced distance of 1 km from the vent to the sensor. This was calculated following the methods described in Le Pichon et al. (2012, 2019) and Tailpied et al. (2017). As a result, a transfer function was estimated for each source/station pair, accounting for both realistic atmospheric specifications along the propagation path and source frequency. The temporal and spatial variability of the atmosphere was described using the ECMWF's (European Centre for Medium-Range Weather Forecasts, part of the Integrated Forecast System cycle 38r1, http://www.ecmwf.int/) ERA5 reanalysis or operational High spatial RESolution forecasts (HRES). This includes the winds and temperatures between 30 and 60 km altitude. Additionally, uncertainties from the transfer function are estimated by adding a perturbation of 5% on the wind speed in our calculations (Tailpied et al., 2017; Le Pichon et al., 2019). It is worth noting that this 5% factor was assessed according to previous campaign measurements referred to in Tailpied et al. (2017) and Le Pichon et al. (2019), it is not a fixed value and may vary depending on the time of the year and region of interest. By correcting the amplitude recorded at the sensors (Amp_{data}) for the transmission loss calculated (Att_{calc}), we obtain the amplitude at the reduced distance of 1 km from the vent. The geometric spreading model can then be used to return the values at the source. This leads to the modified equation for the overpressure, ΔP_R, on the regional scale:

$$\Delta P_R(t)^2 = \left[A_{ref} 10^{\frac{(Amp_{data}(t) + |Att_{calc}|)}{20}} \right]^2 \tag{4}$$

where A_{ref} is a nominal reference amplitude of 20×10^{-6} Pa (Garces, 2013), or the value used in the processing of the data and atmospheric modeling. Amp_{data} is the data amplitude in decibels (dB) from the single frequency band at the regional station, and Att_{calc} is the calculated attenuation between the reduced distance of 1 km from the source and the sensor/array (also in dB and usually calculated as a loss). This modified term can then be applied within Eq. (1), and both local and regional methodology will be identical from this point. Eq. (1) can therefore be re-written in terms of local infrasound processing (Eq. (5)), and regional infrasound for distances greater than 100 km (Eq. (6)):

$$\Pi_{aL}(t) = \gamma \pi r^2 \frac{1}{\rho c \tau} \int_{t_i - \tau}^{t_i} | p(t) - p_{air}|^2 dt \tag{5}$$

$$\Pi_{aR}(t) = \gamma \pi r^2 \frac{1}{\rho c} \left(A_{ref} * 10^{\frac{(Amp_{data}(t) - |Att_{calc}|)}{20}} \right)^2 \tag{6}$$

where Eq. (5) is the standard definition of local infrasound acoustic power ($\Pi_{aL}(t)$), with r as the source to sensor distance, and Eq. (6) is the new relationship for regional infrasound acoustic power ($\Pi_{aR}(t)$), incorporating Eq. (4), where r is the reduced distance of 1 km from the vent. All further calculations assume that the background and any noise have been taken into account and removed from the signal as part of ΔP calculation in Eqs. (2) and (4).

2.2. Source radiation patterns: assumptions and source parameter calculations

By calculating acoustic power at the vent, the relationships previously established by Woulff and McGetchin (1976) and based on Lighthill (1952) can be used to calculate the exit velocity. These relationships are highly dependent on the three radiation patterns: monopole, dipole, or quadrupole. Acoustic power can therefore be used to calculate exit velocity with the following equations, depending on the chosen radiation pattern:

$$monopole : \Pi_m = K_m \frac{\pi R^2 \rho_{air} v^4}{c} \tag{7}$$

$$dipole : \Pi_d = K_d \frac{\pi R^2 \rho_{air} v^6}{c} \tag{8}$$

$$quadropole : \Pi_q = K_q \frac{\pi R^2 \rho_{air} v^8}{c} \tag{9}$$

where K_m, K_d, and K_q are empirical constants, R is the vent radius, ρ_{air} is the density of air, c is the speed of sound, and v is the exit velocity at the vent. K_m is of the order of 1 (Vergniolle and Caplan-Auerbach, 2006; Caplan-Auerbach et al., 2010). We used a value of 1 since it is the exact solution for a spherical source, while for a circular flat orifice, K_m would be 1/16, which we will not consider since it is not realistic for a volcanic source. In several previous studies there is an additional multiplicative factor of 4 included in the monopole radiation that can be included within K_m (Vergniolle and Caplan-Auerbach, 2006; Caplan-Auerbach et al., 2010; Lamb et al., 2015). For a dipole source, Woulff and McGetchin (1976) gave a range for K_d from 10^{-2} to 10^{-1}, and stated that 1.3×10^{-2} is the exact solution of highly idealized Aeolian tone, while 10^{-2} originated from experiments by Leehey and Hanson (1970) on an idealized case of jet flow past a taut wire (Matoza et al., 2013). Vergniolle and Caplan-Auerbach (2006) use a value of 1/3 for this constant, and Caplan-Auerbach et al. (2010) and Lamb et al. (2015) both use a nominal value of 10^{-2}. K_q is estimated between 3×10^{-5} and 10^{-4} (Woulff and McGetchin, 1976), and a nominal value of 10^{-5} is used by Caplan-Auerbach et al. (2010) and Lamb et al. (2015), which originated from early jet noise experiments (Matoza et al., 2013). All values for these constants are listed in Table 1. Woulff and McGetchin (1976) describe these three radiation patterns as noise arising from a time varying mass flux (monopole), noise due to the fluid interaction with solid boundaries (dipole), and noise due to jet turbulence (quadrupole). However, Matoza et al. (2013) found that the difference between volcanic jet noise and pure air jet noise is significant enough that large errors are introduced when using Woulff and McGetchin (1976) for volcanic jets. This should be taken into consideration for any local infrasound calculations. Nonetheless, a monopole is generally assumed for long range propagation (Fee et al., 2010; Dabrowa et al., 2011). The radiation pattern Eqs. (7)–(9) were generalized by Matoza

et al. (2013) into one scaling equation relating the infrasound acoustic power to the exit velocity by:

$$v = \left(\frac{\overline{\Pi}}{c^{3-m}K\rho_{air}\pi R^2}\right)^{\frac{1}{m}} \tag{10}$$

where $\overline{\Pi}$ is the total acoustic power of the source, K is a constant (a generalized version of K_m, K_d, and K_q), and m can be set to 4, 6, or 8 to reproduce the equations for a monopole, dipole, and quadrupole respectively. For this study we are concerned with long range propagation and therefore we have chosen $K = 1$ (monopole) (Dabrowa et al., 2011). This methodology is based on the pioneering work of Lighthill (1952) and Woulff and McGetchin (1976). Recently, a different approach has been used by assuming the source radiation pattern of a multipole with contributions from monopole, dipole, and quadrupole radiation, and relating the source time history of the volume flux directly to the infrasound signal (Kim et al., 2012, 2015; De Angelis et al., 2019; Iezzi et al., 2019). More information on this alternative methodology can be found in the recent review article by De Angelis et al. (2019).

Converting the exit velocity to a volumetric flux is straightforward and can be calculated using:

$$Q = \pi R^2 v \tag{11}$$

where R is the vent radius, and v is the exit velocity. This equation therefore relies on some prior knowledge about the general size of the vent. Depending on the source parameter needed for ash dispersal modeling, the values of exit velocity or volumetric flux can be used directly, or employed to estimate plume height through further relationships and models.

2.3. Plume height from infrasound

There have been several different methods used to estimate a plume height from the parameters derived from infrasonic acoustic power. Following Caplan-Auerbach et al. (2010), we employ two steady-state models that can be used to directly calculate the plume height based on the type of plume: thermal or sustained. A thermally driven plume (smaller, discrete source at the vent) can be estimated using:

$$F_T = Vg\left(\frac{T_0 - T_a}{T_a}\right) \tag{12}$$

$$H_T = 2.7 F_T^{1/4} N^{-1/2} \tag{13}$$

where V is the volume, g is the acceleration of gravity, T_0 is the initial temperature, T_a is the air temperature, $\rho_0(z_{src})$ is the density of the air at the vent, and N is the Brunt-Väisälä frequency:

$$N = \sqrt{-\frac{g^2}{c^2} - \frac{g}{\rho_0}\frac{d\rho_0}{dz}} \tag{14}$$

which can be calculated from the atmospheric vertical density profile $(\frac{d\rho}{dz})$. Caplan-Auerbach et al. (2010) use a value of 0.003 Hz. Thermal plumes are expected to be detected only by local infrasound, but ideal attenuation conditions could lead to detection at further ranges. For sustained plumes, the thermally driven model does not hold, as the plume is fed at the source and is no longer rising due to the thermal gradient of a single volume released. There are two empirical relationships used in plume modeling, Sparks et al. (1997) and the updated Mastin et al. (2009) equations:

$$\text{Sparks et al. (1997)}: H_t = 1.67 Q_m^{0.259} \tag{15}$$

$$\text{Mastin et al. (2009)}: H_t = 2.00 Q_m^{0.241} \tag{16}$$

where the height of the plume H_t is related to the ash volume flux Q_m of the eruption. Both equations use a volumetric flux of pyroclasts instead of a total volumetric flux of pyroclasts and gas and therefore requires an assumption on proportion of gas vs pyroclasts within the plume. A range of 1–15% volume of pyroclasts within the total plume was used by Caplan-Auerbach et al. (2010) to estimate the needed volumetric flux of pyroclasts. Although this value is still not well defined, it is a known unknown and thus contributes to the uncertainties in the final calculation.

Instead of relying on empirical relationships with additional assumptions, Lamb et al. (2015) used the mathematical model PlumeRise (https://plumerise.bristol.ac.uk/), which is based on the fluid dynamics of turbulent buoyant plumes, and has an input for exit velocity (m/s) or mass flux (kg/s) (Woodhouse et al., 2013). This model can also account for the effects of local winds and different plume dynamics, like a "bent over" geometry, which will have a significant impact on the calculated height. While Eqs. (13), (15), and (16) do not take into account local atmospheric conditions, like wind strength and direction, this workflow can easily be implemented into a script and run in an automated fashion. This may be more important for smaller locally recorded plumes, but less important for the larger plumes. For this study, it is assumed that only the larger sustained plume eruptions will generate a large enough infrasound signal to be recorded over a regional scale, and therefore only Eqs. (15)–(16) are applicable, and the impact of local winds less important.

This method was developed with its operational use in mind. It relies on relationships and equations that can be easily implemented and run in a timely manner (see Discussion); each section of the process Fig. A.1 can be replaced as new developments are published.

3. Data and results

3.1. Data collection and signal identification

Infrasound data for this project were recorded by infrasound arrays located within the SE Asia region. All of these arrays are part of the IMS with the exception of the non-IMS array in Singapore (SING) which was also analyzed. The IMS infrasound network was designed to detect and locate any atmospheric explosion with a yield of 1 kt or greater, anywhere on the planet (Christie and Campus, 2010). The network will eventually consist of 60 arrays worldwide, at the time of writing, 52 out of 60 arrays have been installed and certified. The average spacing between arrays is 1902 km on the Northern hemisphere and 2027 km on the Southern hemisphere. The IMS infrasound arrays have an average array aperture of 2 km, and consist of four to eight microbarometers certified with a flat response between 0.02 and 4 Hz (Christie and Campus, 2010). The sensors sample the pressure field in the direct vicinity of the array element at 20 Hz. Additionally, wind noise reduction systems are in place to filter out incoherent pressure fluctuations that are due to the wind.

Once recorded, the data are telemetered to the International Data Center (IDC) in Vienna Austria. In at least 97% of the time, data should arrive within the allowable time delay of 5 min (Christie and Campus, 2010, following consultation of IMS documentation). For the purpose of this study, we used data from the following stations: I22FR Port Laguerre in New Caledonia, I52GB Diego Garcia in the Chagos Archipelago, I05AU Hobart in Tasmania, I04AU Shannon in Australia, I06AU in Cocos Island, I39PW in Palau, and I07AU Warramunga in Australia (Fig. 1, Table 2). Coherent acoustic signals were identified through array processing using, the Progressive Multi-Channel Correlation (PMCC) program (Cansi, 1995), and further processing was completed with waveform analysis described below. The timing and location of the eruption was known, and these values were used to calculate an expected arrival time and backazimuth for each station, and to identify and isolate the event signal. For some of the array processing results additional treatment was required to identify the signal. For example, in
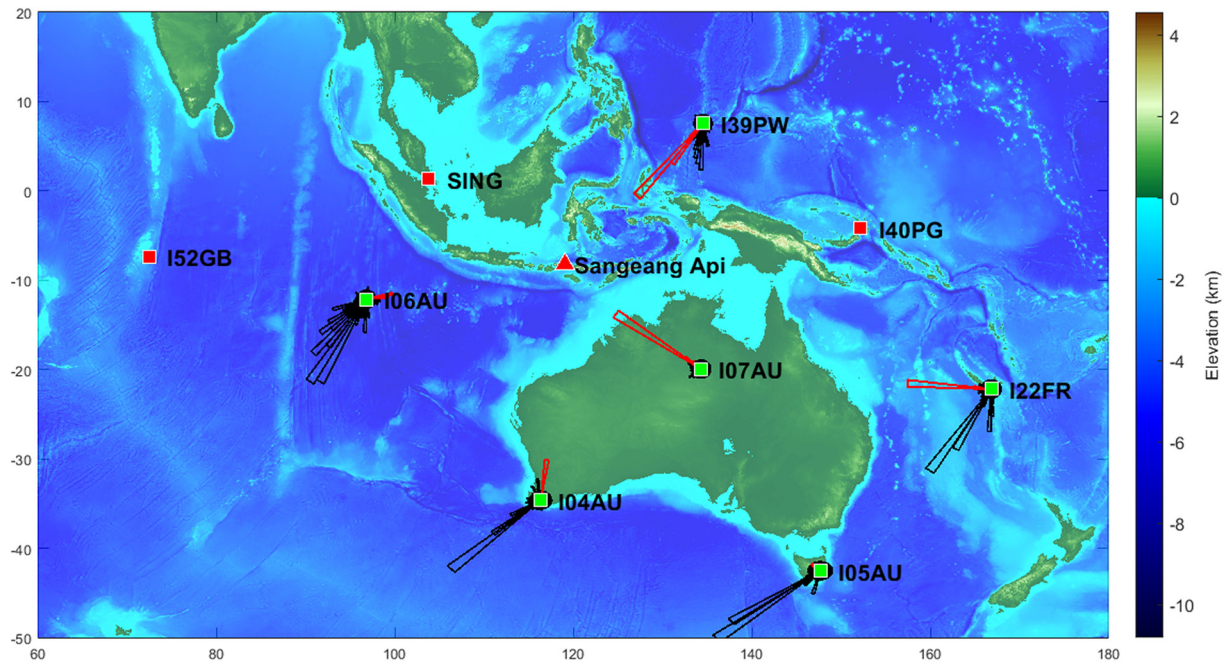
Fig. 1. Location of the volcano Sangeang Api relative to the Infrasound arrays used for this analysis. Arrays that detected the eruption are plotted in green, and arrays with no detection or no data are plotted in red. Array processing results are plotted as a rose diagram for each detecting station, and normalized to the maximum number of detections in 5 degree bins per station ranging from 456 km for I06AU, to 6543 km for I07AU. For each station the detections are filtered in time, based on the time of the eruption and a range of celerities from 0.25 to 0.45 km/s. All detections within ±10 degrees of the calculated backazimuth are plotted in red and all other detections from other infrasound sources at the time are plotted in black. (For interpretation of the references to colour in this figure legend, the reader is referred to the web version of this article.)

order to identify the signal recorded at I06AU, spectral subtraction was used to remove the coherent microbarom signal which was interfering with the detection of the Sangeang Api signal (Williams et al., 2020). Once this analysis was completed, the array processing was able to distinguish the volcanic signal at I06AU.

3.2. Case study: the 2014 eruption of Sangeang Api volcano

Sangeang Api, a small 13 km wide island NE of Sumbawa island, is one of the most active volcanoes within the Lesser Sunda islands in Indonesia (Global Volcanism Program, 2014b). After a period of

elevated seismicity in early 2014, Sangeang Api erupted on May 30th, 2014, at 07:55 UTC, causing local evacuations. CVGHM initially reported the plume to be 3 km on May 30th, this was followed at 09:45 UTC by the first VAAC report, which indicated that a plume was seen in satellite imagery and reported by the Indonesian Met Office to 10 km (FL350) (Global Volcanism Program, 2014a). A second report at 10:30 UTC mentioned that a high-level eruption was observed in satellite imagery and confirmed by Indonesia Met Office to 15.2 km (FL500). See Fig. 2 for a timeline of events (Global Volcanism Program (GVP) and VAAC). This eruption sequence was a series of large explosions: the initial eruption at 07:55 UTC was followed closely by a second on May 31st at 05:30

Table 2

The known volcano (Sangeang Api) and eruption time (07:55 UTC), and range to each station was used to calculate a known expected arrival time based on a propagation speed of 300 m/s standard for stratospheric arrivals. Included also is the actual reported arrival time of the signal, and its duration. The calculated backazimuth is reported along with the deviation from that backazimuth from the array processing results. The signal amplitude at the chosen frequency band of 0.1 Hz is reported as a range for each array and from the array beam waveform. The attenuation values are reported, along with their uncertainties. These were supplied and calculated separately from this study. The mean acoustic power is reported along with the acoustic power, assuming geometric spreading. The array beam was then used to calculate the velocity and plume height a.s.l. and again a value for a geometric spreading calculation is also presented. Array beam calculation results are based on geometric spreding factor = 1, and a monopole without the ± on the attenuation.

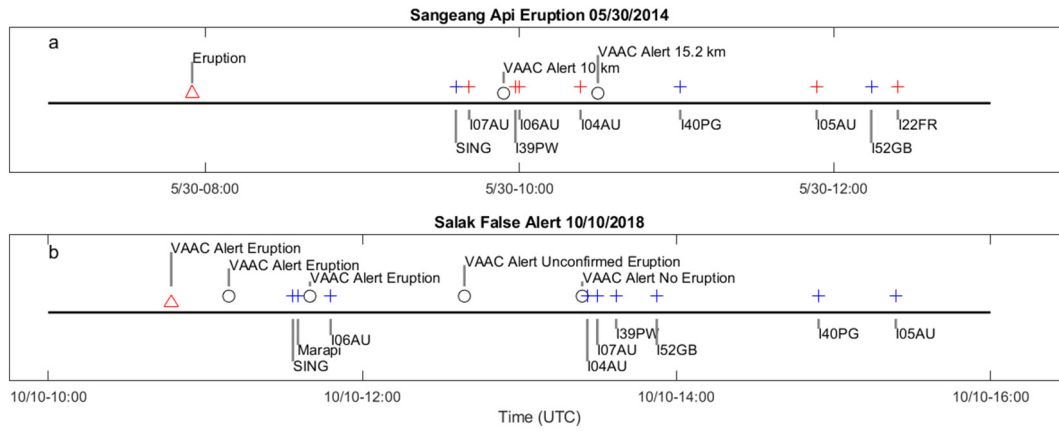| Station	SING	I07AU	I39PW	I06AU	I04AU	I40PG	I05AU	I52GB	I22FR
Range (km)	1995	2096	2445	2476	2938	3692	4723	5137	5338
Calculated azimuth (°)	122	306	225	82	6	261	315	94	279
Expected arrival time 05/30/2014 (300 m/sec)	9:45	9:51	10:10	10:12	10:38	11:20	12:17	12:40	12:51
Observed arrival time		9:31	10:10	10:05	10:38		12:02		12:30
Signal duration (min)		64	42	33	25		40		51
PMCC Az ± (°)		302 ± 0.01	222 ± 0.01	79 ± 0.19	6 ± 0.05		340 ± 0.34		272 ± 0.01
Signal amp. at 0.1 Hz (dB)		80–81	70–72	81–85	78–83		69–70		76–78
Beam amp 0.1 Hz		80	71	82	82		69		77
Attenuation at 0.1 Hz (dB)	−63	−61	−66	−67	−65	−60	−68	−60	−63
Attenuation uncertainties (dB)	3.46	3.55	3.93	3.54	3.93	3.39	3.77	3.38	3.5
Mean acoustic power (with attenuation)		1.57E+09	0.67E+09	11.96E+09	5.22E+09		0.68E+09		0.96E+09
Beam acoustic power (without attenuation)		10.09E+09	1.15E+09	7.32E+09	4.59E+09		0.18E+09		0.7E+09
Array beam velocity (m/s)		63	51	96	84		49		56
Height (array beam Mastin et al. (2009), 4%)		18.9	18.1	20.7	20.1		17.9		18.4
Height array beam range (1–15%)		14–25	13–24	15–28	15–27		13–24		14–25
Height (array beam Mastin et al. (2009), 4%, without attenuation)		22.2	19.7	21.8	21.3		17.9		19.2

Fig. 2. Timeline figure for Sangeang Api and Salak volcanoes. A: Timeline of events for the Sangeang Api eruption. The eruption time is plotted as a red triangle, the expected arrival times across the infrasound array network are plotted as a blue cross, and if the signal was detected it is plotted as a red cross, and the VAAC alert times are plotted as black circles. The final height of the plume was not reported until the second VAAC alert and before that there was the possibility of a detection being recognized at five infrasound arrays. B: Timeline of false alert for Salak volcano following the same conventions. In this case the VAAC reported a high-level eruption and then withdrew the alert. (For interpretation of the references to colour in this figure legend, the reader is referred to the web version of this article.)

UTC and a third eruption at 14:42 UTC the same day. This phase of activity lasted until mid-June 2014. Prior to this eruption, the recent eruptive activity included small explosions in 2009, with the last significant eruptions occurring in 1997–1999. The later included explosive activity, lava domes, and lava discharge (Global Volcanism Program, 2014b).

The eruption on May 30th, 2014, at 07:55 UTC, produced a clear, strong infrasound signal (Fig. A.2) that was recorded by the IMS infrasound network on stations I07AU (2096 km), I39PW (2445 km), I06AU (2476 km), I04AU (2938 km), I05AU (4723 km), and I22FR (5338 km) (Figs. 1, A.3), with an estimated origin time of 07:57 UTC taken from the Reviewed Event Bulletin (REB) published by the CTBT Organization. The eruption plume was also observed locally and via satellite. In addition to the observations and plume height estimations at the time of the eruption, subsequent work has been done on the satellite detections to calculate the plume height (Zidikheri et al., 2017), making this event ideal for examination of different techniques for remote plume height estimation. We will use the observational heights, as well as the heights derived from post-processed satellite, as a comparison for the heights calculated from the infrasound signals through our method. The height of the plume was reported between 15 and 20 km, and Zidikheri et al. (2017) calculated a height of 19.0–21.0 km above sea level with an optimal top height of 20 km.

Array processing results from PMCC were examined to determine if any "pixels" (detections) were consistent with the expected arrival time, azimuth, and apparent velocity originating from the known source. PMCC is an array processing algorithm that estimates wavefront parameters like backazimuth, and apparent velocity using correlation and time delays between array elements. This is calculated over several frequency bands with independent time windows. The algorithm outputs pixels of detections with these parameters within individual windows of frequency and time, and groups these pixels into families with similar wavefront properties (Cansi, 1995). PMCC was configured using 3rd octave band spacing, with window lengths scaled by frequency, following the INFERNO method (Garces, 2013, Table B.1). Due to the uniformity of IMS stations, the same configuration was used for all of them. Once a station was determined to have detected the event, the signal itself was analyzed. The period of highest energy was calculated using INFERNO frequency band analysis, and was consistently found to be 10 s, or 0.1 Hz, across the region. This frequency band was thus chosen for attenuation analysis, and the maximum amplitude within this frequency band was calculated for each site within each array. In addition to the recorded signals, an array beam for each array was constructed using the known backazimuth and an apparent

velocity across the array of 340 m/s. The maximum amplitude within the chosen frequency band was also calculated from the array beam and used within the analysis (see Table 2, Figs. 3, and A.2).

Infrasound signal attenuation values were calculated between the known source (Sangeang Api volcano) and each array, using ECMWF ERA5 reanalysis of atmospheric specifications (wind and temperature profiles) along the propagation path for the day of the event (Fig. A.4). Associated uncertainties from the wind data were estimated (see Section 2.1.2). The attenuation values were calculated through the attenuation modeling technique previously described. Following Eq. (4), we calculated the source amplitude at a reduced distance of 1 km from the vent using the observed amplitude at each sensor and the array beam (Amp_{data}). The mean source amplitude at the reduced distance of 1 km from the vent was also calculated and was found to be 142 +/− 14 dB at 0.1 Hz (Fig. 3). The acoustic power was calculated following Eq. (6) and the methods outlined in Section 2.1 (Fig. 4). These values were also compared with the results from assuming only geometric spreading (Eq. (5)), as was used in Dabrowa et al. (2011).

The acoustic power calculations were then converted into source parameters following the methods described in Section 2.2. Acoustic power was converted to exit velocity at the vent using Eq. (10), assuming a monopole for the radiation pattern (Table 2 and Fig. 4). The vent radius of 30 m was estimated from satellite images available in Google Earth (Table 2). In order to account for uncertainties surrounding the vent radius linked to the measurement methods and others (ambiguity of where within the vent the radius should be measured, and the eroding and widening of the vent during the eruption), an arbitrary but reasonable error of 10% was added to this value. In order to estimate the plume height from the exit velocity, the pyroclasts volumetric flux was calculated using the geometry of the vent and the fraction of pyroclasts vs. gases within the plume. We have used 1% to 15%, with 4% as a nominal reference value (Caplan-Auerbach et al., 2010). From here, the empirical relationships between pyroclasts volumetric flux and plume height from Sparks et al. (1997) and the updated Mastin et al. (2009) (Eqs. (15) and (16), respectively), were used. These calculations were then compared to both the reported plume height of 13.25 km above the vent from the VAAC report, and the reanalyzed plume height estimated from satellite data within a range of 17.05–19.05 km from Zidikheri et al. (2017) (Fig. 5). Using the nominal 4% ash volume within the plume, the mean plume height above the vent from all stations is 18.4 km with a range from 14.9 to 23.6 km, which is well within the range of reported and reanalyzed values (Fig. 5).
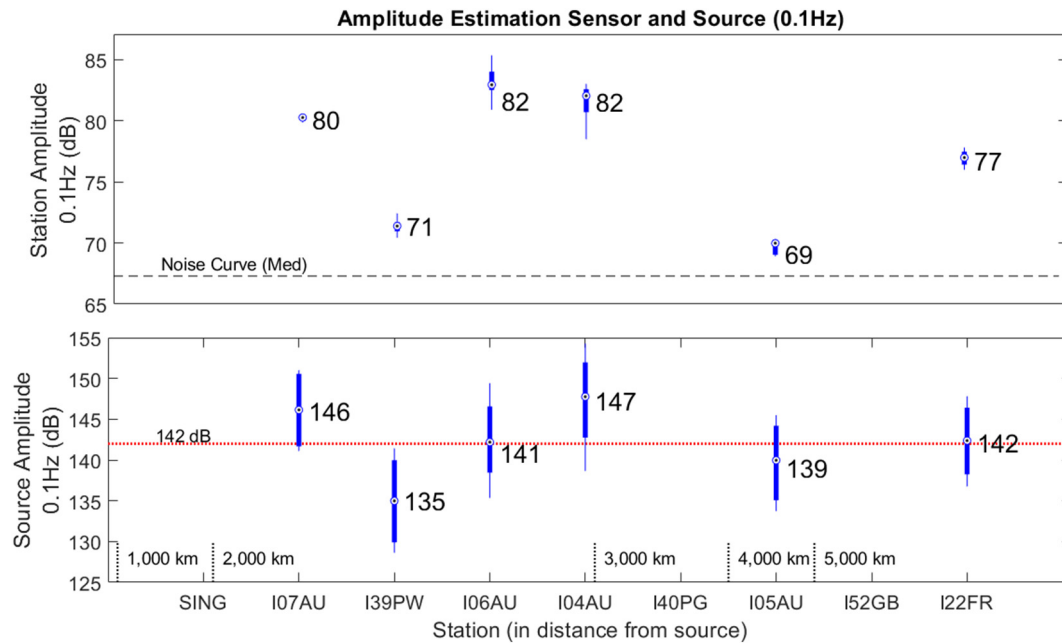
Fig. 3. Top: calculated amplitudes for the dominant frequency of 0.1 Hz. The range of measurements for each element is plotted as box plots with the highlighted area representing the range from the 25th to 75th percentiles, and with the whiskers representing the full range of measurements and with the value for the array beam noted for each array. Bottom: The atmospheric attenuation and associated uncertainties have been added to the measured values to estimate the source amplitude. The horizontal dotted line represents the mean value retrieved for the source amplitude at 142 dB at 0.1 Hz.

4. Discussion

4.1. Remote infrasound monitoring of volcanoes

This paper presents a novel approach to regional plume height estimation by bringing together methods previously established in infrasound for the local case, atmospheric attenuation modeling, and plume models. Remote sensing of volcanic plumes is dominated by space-based instrumentation, which while effective has limitations based on temporal resolution, cloud coverage, and time of day depending on the system available. Moving towards a combined system of space-based remote sensing, and ground based regional infrasound
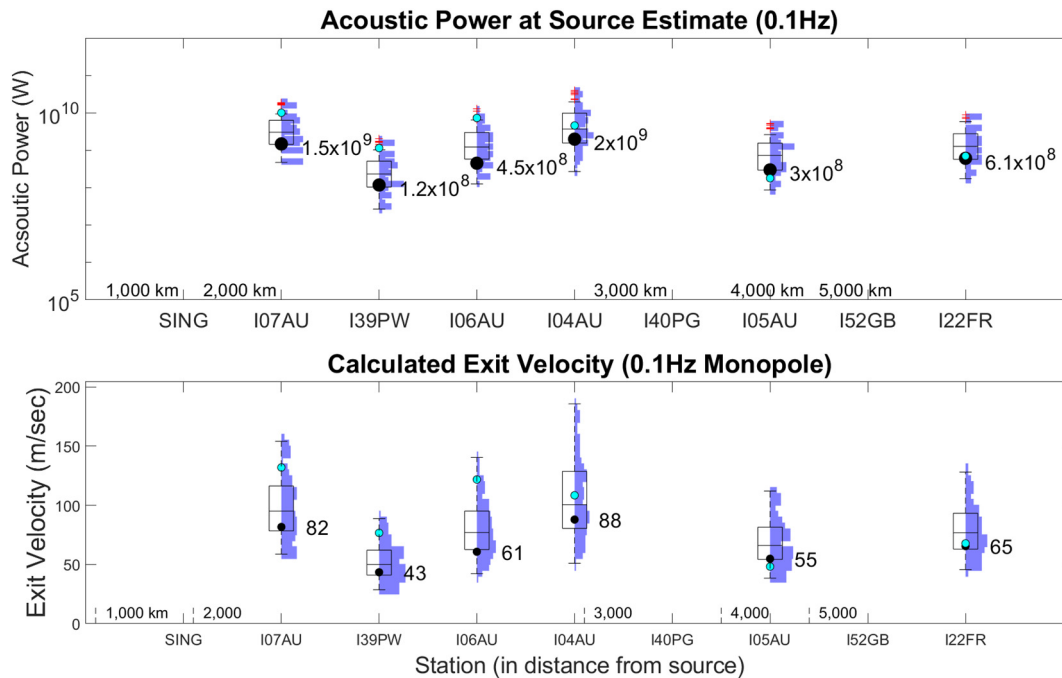

Fig. 4. Top: Acoustic power at the source (vent) as calculated with Eq. (4) including the uncertainties in attenuation, geometric spreading factor, and the amplitude measurements for each element and the array beam amplitude at each array. In order to highlight a single calculation (plotted in black) is the calculation using the amplitude of the array beam at each array value, and the preferred value for all other variables. For comparison, the same calculation using only geometric spreading instead of the attenuation model, is plotted in cyan. Note that while this is a good approximation for some stations, due to the complexities of infrasound propagation through the atmosphere it can deviate significantly, which would propagate through the rest of the calculations. Bottom: Calculated exit velocity, with the preferred values and array beam calculation (black) and geometric spreading (cyan). This calculation also incorporates the uncertainty on the vent radius of 10%. (For interpretation of the references to colour in this figure legend, the reader is referred to the web version of this article.)
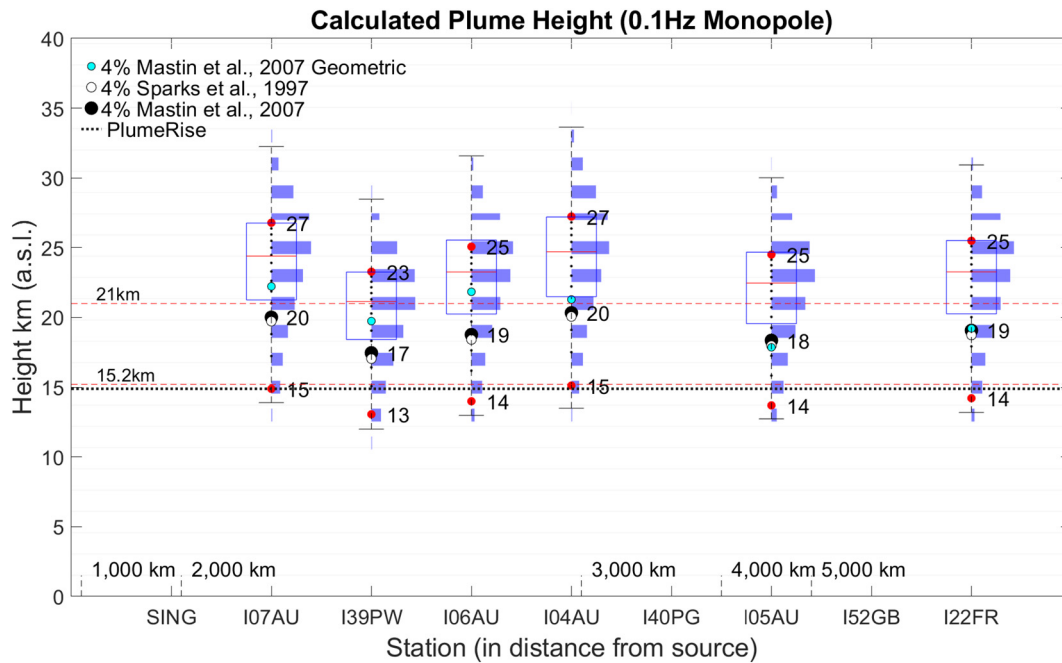
Fig. 5. All plume height calculations for each remote infrasound station that detected the eruption. All results are plotted as a histogram and a box plot. One calculation with preferred values and array beam amplitude as used in the previous figure, plotted for the volume of pyroclasts percentages of 1% (red), 4% (black), and 15% (red) using the Mastin et al. (2009) equation. Also plotted is the 4% for the Sparks et al. (1997) equation plotted in white, and for comparison geometric spreading (cyan). The reported plume heights range from 15.2 to 21 km and this range is highlighted with a dashed red line. All heights are in km above sea level (a.s.l.) and the PlumeRise results (top of plume height from the %50 velocity output of Uninet) are plotted as a black line. (For interpretation of the references to colour in this figure legend, the reader is referred to the web version of this article.)

sensing can lead to a system that is independent of cloud cover and time of day, as well as increasing coverage for regions with sparse satellite coverage. We propose that this method could be used operationally when the ash cloud is obscured by a meteorologic cloud, or when particles are coated in ash making them hard to detect. One of the motivations behind this study is the diversification of potential data streams to enable timely confirmation and characterization of large volcanic eruptions in SE Asia. This would feed into steps to mitigate the impact on aviation, and for communities living downwind from an erupting volcano. SE Asia has a high fraction of cloud cover (Taisne et al., 2019), and due to the high moisture content in the atmosphere, ice coating on particles is also an issue for identifying volcanic ash using space-based remote sensing techniques. Therefore, the authors believe that incorporating infrasound into the regional monitoring system would improve the current early warning system, especially for the aviation industry.

The methods presented here can be implemented in near real time, while requiring very little in the way of computational resources, a-priori knowledge, or new infrastructure. The process is also modular and each module could be independently updated as new research is published (Fig. A.1). However, one limitation to the methodology is that it is based on a strong assumption that the signals recorded at distant stations are representative of the total acoustic power of the source. In the nearfield, where radiation is more complex, this assumption might not hold, especially due to the impact of topography, non-linear propagation and source dynamics. In this case, the station geometry is an important factor, and a dipole, or multipole, might be more representative. However, for regional-to-global distances, it has been established that a volcanic eruption acoustic source can be approximated by a monopole and propagation is expected to be linear in nature (Fee et al., 2010; Dabrowa et al., 2011).

In an operational context the main obstacle would be the calculation of the attenuation for a specific source-to-sensor pair. Ideally, atmospheric data both reanalyzed and forecast would be available. If this is the case, the process as described in Section 2.1.2 takes only around a minute to run. Another option would be to undertake a multi-year

study on the variation of attenuation between any point within a study area and an infrasound array (or station) to obtain yearly, or ideally monthly, nominal values with associated uncertainties for estimation. However, if no sufficient atmospheric data are available, geometric spreading could be used as a quick first approximation (Dabrowa et al., 2011). Obtaining quick estimates for plume height, time, and event duration, especially when other observations are not available, would allow for the initiation of ash dispersion models and expedite the issuing of alerts for the aviation industry or communities downwind. This information could be used in-lieu and/or in addition to satellite determinations of the plume. Infrasound has the potential to be used as a first estimate, which could then be refined through time as more information becomes available, similarly to how tsunami warning systems are designed with an initial trigger, and assimilation of additional data as it becomes available. In the case of the 2014 Sangeang Api eruption, it is worth noting that there were two possible infrasound detections before the initial VAAC alert was issued at 09:45 UTC, with the lower height of 10 km. With a total of five possible detections before the VAAC updated its alert with a more accurate plume height at 10:30 UTC, around 2.5 h after the eruption.

Due to the many complications in satellite detection of volcanic plumes, it is not realistic to rely on only one technology for remote volcano monitoring. While infrasound can certainly be used to aid in the detection of eruptions, especially those obscured by clouds, it could also be used as an alternate source of data to potentially identify false detections from satellite data. On October 10th, 2018, a VAAC alert was issued for a high-level eruption at Salak volcano based on satellite data. In reality, a meteorologic cloud was doing a remarkably good impression of a volcanic plume. Several flights were cancelled or diverted due to the alert (AirAsia Indonesia, 2018). Between the time of the first alert, which reported a high-level plume, and the retraction, around two and a half hours later, three infrasound stations should have picked up a strong detection given the size of the reported event and their proximity to the volcano (Fig. 2). The lack of detected infrasound could have been used to help cast doubt that a high level eruption had occurred at this volcano. While infrasound might not be used as a "smoking gun" for a

Table 3
Uninet configuration table and plume rise results for the Sangeang Api case study. Each variable is listed with the type of distribution used, as well as the value(s) or range of values. A description of the variable is also included.

Variable	Distribution	Values	Description
γ	Discrete values	1, 2, 4 weighted 0.8, 0.1, 0.1	Geometric spreading constant
ρ_{air}	Normal	Mean: 1, SDev 0.01	Density of air (kg/m^3)
c	Normal	Mean: 340, SDev 10	Sound speed (m/s)
r	Discrete	1 km	Sensor to source distance (m)
R_{vent}	Normal	Mean 30, SDev 3	Vent radius (m)
m	Discrete	4 (monopole)	Radiation pattern exponent
K	Triangular	a: 0.06, m: 1, b: 1.06	Radiation pattern constant
A_{ref}	Discrete	$2e^{-5}$	Reference atmospheric pressure (Pa)
P_{cet}	Triangular	a: 0, m: 0.03, b: 0.1	Percentage of pyroclasts in plume
P_{src}	Normal	Mean: 141.97, std.: 5.82 (from data)	Source amplitude with attenuation error (dB)

false alarm, in a similar situation, the lack of infrasound coupled with the absence of unrest prior to the event at the volcano, might have expedited the recalling of the VAAC alert.

4.2. Uncertainties

In addition to the calculations described above and carried out in MATLAB, an uncertainty software and plume model were also used as a comparison. Uninet (https://lighttwist-software.com/uninet/), a standalone uncertainty analysis software package for stochastic modeling and multivariate ordinal data mining, was used. It allows for the generation of a large distribution of values for each parameter with various distribution types. All the equations and variables within the methodology, described in Section 2, were input and given a distribution of uncertainty based on a-priori knowledge. Uninet distribution settings and results, are listed in Table 3. Uninet was configured using the source amplitude calculations and the results were fed into the online plume model PlumeRise (Woodhouse et al., 2013), which was used by Lamb et al. (2015). This allowed for consideration of the atmospheric conditions on plume geometry. The atmospheric profile for the time of the eruption was derived from ECMWF ERA5 reanalyzed atmospheric profiles, and input into PlumeRise to account for any bending of the

plume due to winds. The resulting plume heights, based on the 5th, 50th and 95th percentiles, were all within the range of reported heights (Fig. 6, Table 4), and the atmospheric conditions indicate minimal bending of the plume. These results are consistent with the VAAC reported height of 15.2 km, and the calculated heights using a lower mass fraction. While the methodology described within this paper does not take into account the bending of plumes, this is likely to occur mostly at high wind conditions and with weaker plumes (Degruyter and Bonadonna, 2013).

4.3. Example workflow for implementation

On January 12th, 2020, there was an eruption from the volcano Taal, in the Philippines (Global Volcanism Program, 2020). This eruption was recorded by the IMS station I39PW, located 1650 km to the east. Based on the known source time and location, the infrasound data were analyzed and the event signal identified. This infrasound signal was then used to estimate a plume height and duration for further ash dispersion modeling (Fig. 7). For the processing, the following steps were used. First, array processing was completed using dtk-PMCC with 3rd octave bands (21 in total) from 0.01–5 Hz (Table B.1) by an hourly automated process. Subsequent calculations could be automatically triggered but, during January 2020, the system was still manually initiated. Strong detections began at the station around 8:22 UTC on January 12th and tapered off to around 22:35 UTC the same day. Second, an array beam was calculated based on the array processing detections and used for further calculations. One-hour segments of the array beam data were filtered based on the frequency content of the array processing within that window. Finally, plume height calculations were completed using both geometric spreading, and the calculated attenuation between Taal and I39PW based on forecast atmospheric data for the day of the event (Fig. A.5). Using these two approaches allowed for comparisons of final outcomes between forecast atmospheric data, and if geometric spreading had been used because the atmospheric data were not available available. The maximum amplitude within the one-hour processing window was back-propagated to the reduced distance of 1 km from the vent using the attenuation model (Eq. (6)), and the plume height was calculated from Mastin et al. (2009) (Eq. (16)). These results were compared with the measured values of 16–17 km from the Himawari-8 satellite (Prata, 2020), and the heights of 16 km reported by the Tokyo VAAC. While the error bars based on the mass loading
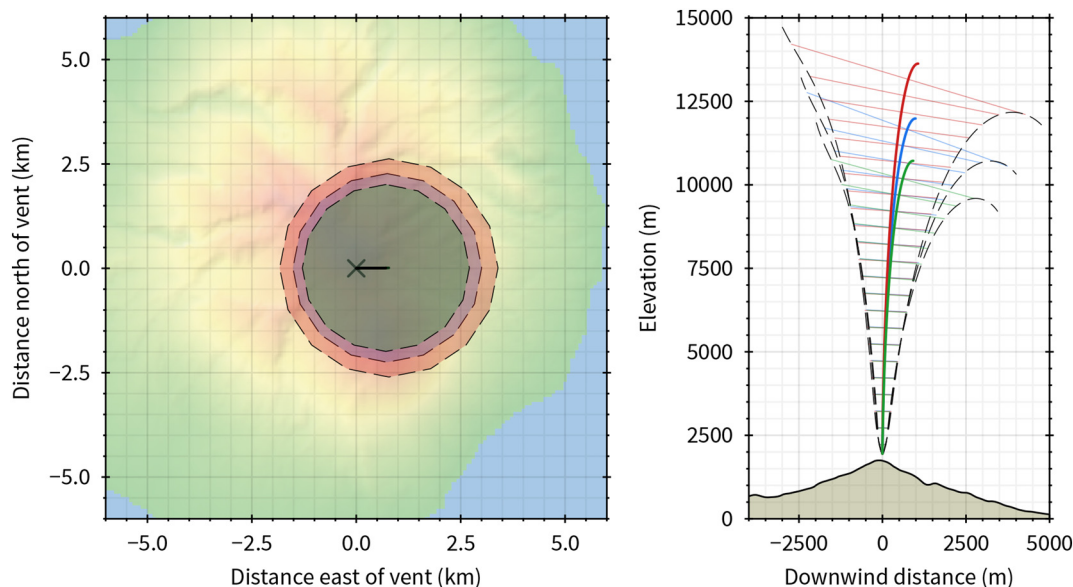

Fig. 6. Results from PlumeRise from the exit velocity calculated from UniNet with the 5% plotted in green, the 50% plotted in blue, and the 95% plotted in red. The results for the centerline height, and top of the plume are located in Table 4. (For interpretation of the references to colour in this figure legend, the reader is referred to the web version of this article.)

Table 4
PlumeRise and Uninet results for the Sangeang Api eruption case study.

Variable	Values and units	Description
V	5%: 58.811 m/s 50% 106.67 m/s 95%: 200.8 m/s	Exit velocity
H_t sparks	5%: 15.4 km a.s.l. 50%: 21 km a.s.l. 95%: 26.5 km a.s.l.	Calculated height using sparks equation
H_t Mastin et al. (2009)	5%: 15.9 km a.s.l. 50%: 21.2 km a.s.l. 95%: 26.4 km a.s.l.	Calculated height using Mastin et al. (2009) equation
PlumeRise height 5% velocity	Centerline height: 10.5 km Top of plume: 13.7 km Neutral buoyancy centerline height: 8.7 km	
PlumeRise height 50% velocity	Centerline height: 12 km Top of plume: 16.1 km Neutral buoyancy centerline height: 9.8 km	
PlumeRise height 95% velocity	Centerline height: 14 km Top of plume: 19.4 km Neutral buoyancy centerline height: 11.3 km	

within the plume are large, the preferred value of 4% provided a good estimation of the plume height with both the atmospheric data, and geometric spreading, with a mean of 15 km and a maximum of 17 km. Both the infrasound and the satellite observations were able to characterize the initial increase in plume height and the subsequent reduction. Towards the end of the eruption, the plume was obscured by a meteorological cloud, and the infrasound indicates that, while it cannot be observed, the energetic phase of the eruption had also ended, thus also providing insight into the plume dynamics.

With the exception of the time it takes for the signal to travel from the source to the sensor (in this case around 85 min), the most time-consuming aspect of this process was the temporal spacing of the array processing calculations. While the specific installation that was used is run hourly, the time between each array processing calculation could be shortened. With the current configuration, the process from array processing (1 min per array) to final plume height (calculations in less than 5 min) can produce usable results in a timely manner. In this case, the atmospheric forecast was pre-calculated but took only 1.5 min to run, and geometric spreading could also be used (as illustrated in Fig. 7) if atmospheric data was unavailable. The first VAAC alert was issued at 07:19 UTC for a 1.5 km plume, a second alert was issued at 07:54 UTC with the same height. At around 08:22 UTC, a strong infrasound signal arrived at I39PW, and the VAAC later issued an alert at
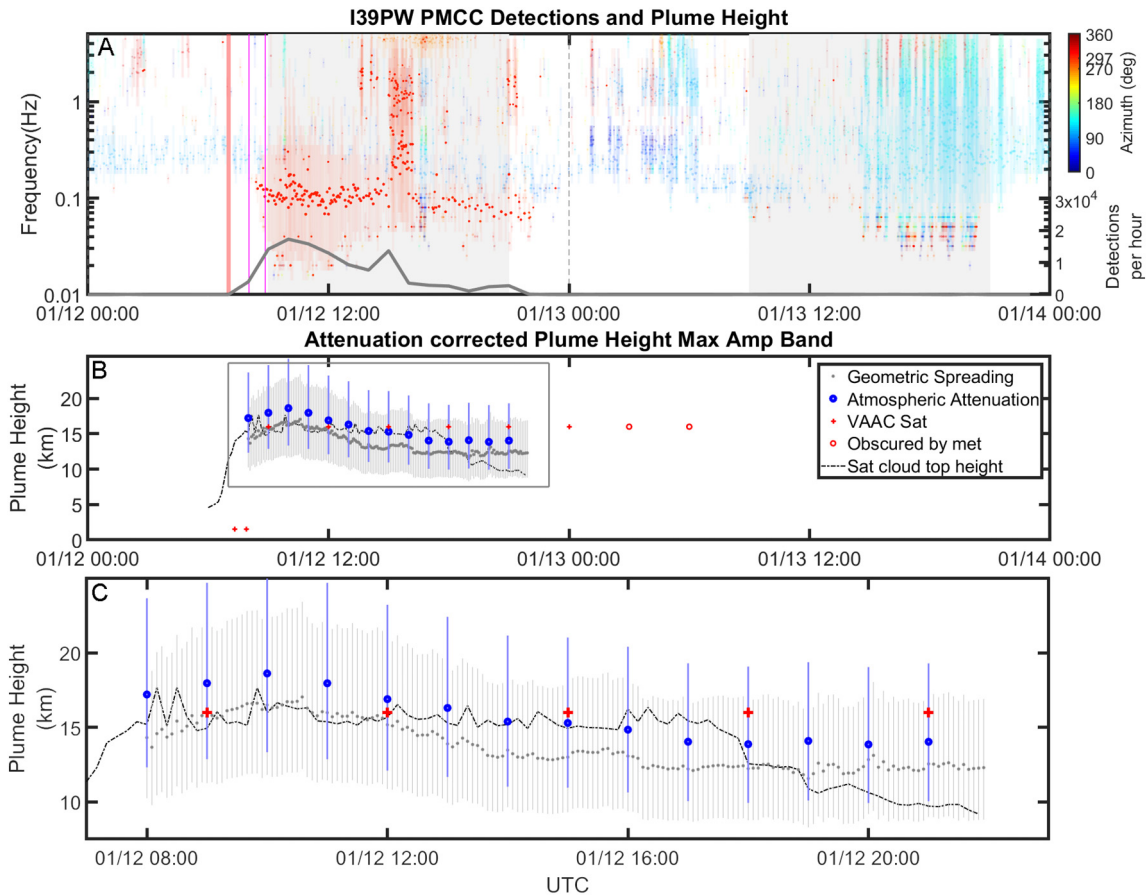

Fig. 7. A: Results for Taal array processing using PMCC from I39PW located 1650 km east of the volcano. The array processing results are plotted as vertical lines from the minimum to maximum frequency per family, with the mean frequency of that family plotted with a dot. Highlighted with darker dots are the families ±10 degrees from the calculated backazimuth of 297 degrees. This allows for variation in azimuth due to propagation effects and errors due to array geometry. In the bottom of the top panel is a gray line showing the number of pixels per hour within this threshold. The vertical light red line represents the eruption time at the volcano, and the magenta lines illustrate the expected arrival time of infrasound based on that eruption time, the distance from source to sensor, and a range of celerities from 0.25 to 0.45 km/s. B: Estimated plume height is plotted. First the plume height was estimated using geometric spreading when the number of pixels per hour from the volcano exceeds the threshold of 500. This estimation is plotted from 1 to 15% with the 4% value highlighted through time. On top of that is the estimation using the attenuation and regional method presented in this paper. The attenuation is calculated from forecast data. The band chosen for each hour window is the closest band to the band of maximum energy within the frequency window defined by the PMCC families. Again, the results are plotted with 1–15% with the 4% highlighted in blue. Also plotted is an estimation of plume height of the umbrella cloud from satellite-based data on cloud top temperature as dotted lines. The reported heights from the Tokyo VAAC are in red. C: Zoom in on the intense phase of the eruption (denoted in B with gray box) reproduced to highlight details. (For interpretation of the references to colour in this figure legend, the reader is referred to the web version of this article.)

09:00 UTC, with the height of 16 km. Even allowing for the travel time of around 85 min, the maximum allowable signal delay of 5 min for an IMS infrasound station, and the processing time of around 8 min, the plume height could have been calculated before this VAAC alert. This is even more noticeable for the Sangeang Api 2014 eruption when the alert issuing the full plume height occurred 2.5 h after the event, and meanwhile, five infrasound arrays had already detected the event.

5. Conclusions

Infrasound is a powerful tool that can be added to the current arsenal of monitoring techniques used for understanding and forecasting volcanic activity. Forecasting is not restricted to determining the onset and evolution of an eruption, but also its associated impacts. In order to do so, in an operational environment, a timely estimate of the source parameters controlling the eruption's dynamic is essential. The eruption of Taal volcano provided a new case study and example of how these methods can be implemented and automated. The proposed novel method and workflow present an alternative tool, independent of time of day and cloud cover, to estimate the plume height associated with a volcanic eruption. It is based on, and expands from, established local infrasound methods that are computationally simple enough to be included with automated operational processing. While other source parameters are accessible, we concentrate here on the plume height as it is a key input parameter for running ash dispersion models. When run in a timely manner and with high enough level of confidence, the results can be used in forecasting the location of ash in the atmosphere or reaching the ground, through time. Such information benefits not only the aviation industry, but also neighboring communities that can take mitigating action if the information is provided with enough lead time.

CRediT authorship contribution statement

Anna Perttu: Conceptualization, Data curation, Formal analysis, Investigation, Methodology, Software, Visualization, Writing - original draft, Writing - review & editing. **Benoit Taisne:** Conceptualization, Funding acquisition, Project administration, Writing - review & editing, Visualization. **Silvio De Angelis:** Methodology, Validation, Writing - review & editing, Visualization. **Jelle D. Assink:** Resources, Methodology, Writing - original draft. **Dorianne Tailpied:** Resources, Methodology, Visualization, Writing - review & editing. **Ross Adrian Williams:** Resources, Writing - review & editing.

Declaration of competing interest

The authors declare that they have no known competing financial interests or personal relationships that could have appeared to influence the work reported in this paper.

Data availability

CTBT IMS and European Centre for Medium-Range Weather Forecasts (ECMWF) data used for this article are available to member states but can be requested for academic purposes. The CTBT Organization (CTBTO) and IMS station operators are thanked for the high-quality data and products. Infrasound data can be requested at the CTBTO International Data Center (IDC) in Vienna, via the virtual Data Exploration Center.

Appendix A. Supplementary data

Supplementary data to this article can be found online at https://doi.org/10.1016/j.jvolgeores.2020.106997.

References

AirAsia Indonesia, 2018. Travel advisory: AirAsia flights status from and to Jakarta (CGK) 10 October 2018 22:00 HRS LT (GMT+7) — AirAsia newsroom. https://newsroom.airasia.com/news/2018/10/10/travel-advisory-airasia-flights-status-from-and-to-jakarta-cgk-10-october-2018-22-00-hrs-lt-gmt7. (Accessed 3 March 2020).

Aneeka, S., Zhong, Z.W., 2016. NOX and CO2 emissions from current air traffic in ASEAN region and benefits of free route airspace implementation. Journal of Applied and Physical Sciences 2, 32–36.

Assink, J., Waxler, R., Velea, D., 2017. A wide-angle high Mach number modal expansion for infrasound propagation. The Journal of the Acoustical Society of America 141, 1781–1792. https://doi.org/10.1121/1.4977578.

Bessho, K., Date, K., Hayashi, M., Ikeda, A., Imai, T., Inoue, H., Kumagai, Y., Miyakawa, T., Murata, H., Ohno, T., Okuyama, A., Oyama, R., Sasaki, Y., Shimazu, Y., Shimoji, K., Sumida, Y., Suzuki, M., Taniguchi, H., Tsuchiyama, H., Uesawa, D., Yokota, H., Yoshida, R., 2016. An introduction to himawari-8/9—Japan's new-generation geostationary meteorological satellites. Journal of the Meteorological Society of Japan. Ser. II 94, 151–183.

Bowen, J.T., 2016. "Now everyone can fly"? Scheduled airline services to secondary cities in southeast Asia. J. Air Transp. Manage. 53, 94–104.

Cansi, Y., 1995. An automatic seismic event processing for detection and location: the PMCC method. Geophys. Res. Lett. 22, 1021–1024.

Caplan-Auerbach, J., Bellesiles, A., Fernandes, J.K., 2010. Estimates of eruption velocity and plume height from infrasonic recordings of the 2006 eruption of Augustine volcano, Alaska. J. Volcanol. Geotherm. Res. 189, 12–18.

Christie, D.R., Campus, P., 2010. The IMS Infrasound Network: Design and Establishment of Infrasound Stations. Infrasound Monitoring for Atmospheric Studies. Springer, pp. 29–75.

Dabrowa, A.L., Green, D.N., Rust, A.C., Phillips, J.C., 2011. A global study of volcanic infrasound characteristics and the potential for long-range monitoring. Earth Planet. Sci. Lett. 310, 369–379.

De Angelis, S., Diaz-Moreno, A., Zuccarello, L., 2019. Recent developments and applications of acoustic infrasound to monitor volcanic emissions. Remote Sens. 11, 1302.

de Groot-Hedlin, C., 2016. Long-range propagation of nonlinear infrasound waves through an absorbing atmosphere. The Journal of the Acoustical Society of America 139, 1565–1577.

de Groot-Hedlin, C.D., Hedlin, M.A.H., 2014. Infrasound detection of the Chelyabinsk meteor at the USArray. Earth Planet. Sci. Lett. 402, 337–345.

de Groot-Hedlin, C., Blackman, D.K., Jenkins, C.S., 2009. Effects of variability associated with the Antarctic circumpolar current on sound propagation in the ocean. Geophys. J. Int. 176, 478–490.

de Groot-Hedlin, C., Hedlin, M.A., Walker, K., 2011. Finite difference synthesis of infrasound propagation through a windy, viscous atmosphere: application to a bolide explosion detected by seismic networks. Geophys. J. Int. 185, 305–320.

Degruyter, W., Bonadonna, C., 2013. Impact of wind on the condition for column collapse of volcanic plumes. Earth and Planetary Science Letters 377-378, 218–226. http://www.sciencedirect.com/science/article/pii/S0012821X13003646 https://doi.org/10.1016/j.epsl.2013.06.041.

Diaz-Moreno, A., Iezzi, A.M., Lamb, O.D., Fee, D., Kim, K., Zuccarello, L., De Angelis, S., 2019. Volume flow rate estimation for small explosions at Mt. Etna, Italy, from acoustic waveform inversion. Geophys. Res. Lett. 46, 11071–11079.

Edelmann, G.F., Drob, D.P., Lingevitch, J.F., Collins, M.D., Le Pichon, A., 2005. Modeling volcanic infrasound propagation using the parabolic equation. The Journal of the Acoustical Society of America 117 (4), 2421. https://doi.org/10.1121/1.4786475.

Fee, D., Matoza, R.S., 2013. An overview of volcano infrasound: from Hawaiian to Plinian, local to global. J. Volcanol. Geotherm. Res. 249, 123–139.

Evers, L.G., Haak, H.W., 2010. The characteristics of infrasound, its propagation and some early history. In: Le Pichon, A., Blanc, E., Hauchecorne, A. (Eds.), Infrasound Monitoring for Atmospheric Studies. Springer, pp. 3–27.

Fee, D., Garces, M., Steffke, A., 2010. Infrasound from Tungurahua volcano 2006–2008: Strombolian to Plinian eruptive activity. J. Volcanol. Geotherm. Res. 193, 67–81.

Garces, M.A., 2013. On infrasound standards, part 1: time, frequency, and energy scaling. InfraMatics 2, 13–35.

Global Volcanism Program, 2014a. Global volcanism program — report on Sangeang Api (Indonesia) — 28 May-3 June 2014. http://volcano.si.edu/showreport.cfm?doi=GVP.WVAR20140528-264050. (Accessed 20 February 2020).

Global Volcanism Program, 2014b. Global volcanism program — report on Sangeang Api (Indonesia) — February 2014. http://volcano.si.edu/showreport.cfm?doi=10.5479/si.GVP.BGVN201402-264050. (Accessed 20 February 2020).

Global Volcanism Program, 2020. Global volcanism program | report on Taal (Philippines) — 8 January-14 January 2020. http://volcano.si.edu/showreport.cfm?doi=GVP.WVAR20200108-273070. (Accessed 20 February 2020).

Godin, O.A., Naugolnykh, K.A., 2005. Guided propagation of naturally occurring infrasound in the troposphere and stratosphere. Geophys. Res. Lett. 32.

Guffanti, M., Casadevall, T.J., Budding, K.E., 2010. Encounters of Aircraft With Volcanic Ash Clouds: A Compilation of Known Incidents, 1953–2009. US Dep. Int. US Geol. Surv, Reston (VA).

Iezzi, A.M., Fee, D., Kim, K., Jolly, A.D., Matoza, R.S., 2019. 3-d acoustic multipole waveform inversion at Yasur volcano, Vanuatu. J. Geophys. Res. Solid Earth 124 (8), 8679–8703. https://doi.org/10.1029/2018JB017073.

Johnson, J.B., Miller, A.J.C., 2014. Application of the monopole source to quantify explosive flux during Vulcanian explosions at Sakurajima volcano (Japan). Seismol. Res. Lett. 85, 1163–1176.

Johnson, J.B., Ripepe, M., 2011. Volcano infrasound: a review. J. Volcanol. Geotherm. Res. 206, 61–69.

Jolly, A., Kennedy, B., Edwards, M., Jousset, P., Scheu, B., 2016. Infrasound tremor from bubble burst eruptions in the viscous shallow crater lake of white island, New Zealand, and its implications for interpreting volcanic source processes. J. Volcanol. Geotherm. Res. 327, 585–603.

Kim, K., Lees, J.M., 2011. Finite-difference time-domain modeling of transient infrasonic wavefields excited by volcanic explosions. Geophys. Res. Lett. 38.

Kim, K., Lees, J.M., Ruiz, M., 2012. Acoustic multipole source model for volcanic explosions and inversion for source parameters. Geophys. J. Int. 191, 1192–1204.

Kim, K., Fee, D., Yokoo, A., Lees, J.M., 2015. Acoustic source inversion to estimate volume flux from volcanic explosions: ACOUSTIC SOURCE INVERSION. Geophys. Res. Lett. 42, 5243–5249.

Lacanna, G., Ripepe, M., 2013a. Influence of near-source volcano topography on the acoustic wavefield and implication for source modeling. J. Volcanol. Geotherm. Res. 250, 9–18.

Lacanna, G., Ripepe, M., 2013b. Influence of near-source volcano topography on the acoustic wavefield and implication for source modeling. J. Volcanol. Geotherm. Res. 250, 9–18.

Lacanna, G., Ichihara, M., Iwakuni, M., Takeo, M., Iguchi, M., Ripepe, M., 2014. Influence of atmospheric structure and topography on infrasonic wave propagation. Journal of Geophysical Research: Solid Earth 119, 2988–3005.

Lamb, O.D., De Angelis, S., Lavallée, Y., 2015. Using infrasound to constrain ash plume rise. J. Appl. Volcanol. 4.

Le Pichon, A., Ceranna, L., Vergoz, J., 2012. Incorporating numerical modeling into estimates of the detection capability of the IMS infrasound network. J. Geophys. Res. D: Atmos. 117.

Le Pichon, A., Ceranna, L., Vergoz, J., Tailpied, D., 2019. Modeling the detection capability of the global IMS infrasound network. In: Le Pichon, A., Blanc, E., Hauchecorne, A. (Eds.), Infrasound Monitoring for Atmospheric Studies: Challenges in Middle Atmosphere Dynamics and Societal Benefits. Springer International Publishing, Cham, pp. 593–604.

Lechner, P., Tupper, A., Guffanti, M., Loughlin, S., Casadevall, T., 2018. Volcanic ash and aviation—the challenges of real-time, global communication of a natural hazard. In: Fearnley, C.J., Bird, D.K., Haynes, K., McGuire, W.J., Jolly, G. (Eds.), Observing the Volcano World: Volcano Crisis Communication. Springer International Publishing, Cham, pp. 51–64.

Leehey, P., Hanson, C.E., 1970. Aeolian tones associated with resonant vibration. J. Sound Vib. 13, 465–483.

Lighthill, M.J., 1952. On sound generated aerodynamically I. General theory. Proc. R. Soc. Lond. A Math. Phys. Sci. 211, 564–587.

Lingevitch, J.F., Collins, M.D., Siegmann, W.L., 1999. Parabolic equations for gravity and Acousto-Gravity waves. The Journal of the Acoustical Society of America 105, 3049–3056.

Mastin, L.G., Guffanti, M., Servranckx, R., Webley, P., Barsotti, S., Dean, K., Durant, A., Ewert, J.W., Neri, A., Rose, W.I., Schneider, D., Siebert, L., Stunder, B., Swanson, G., Tupper, A., Volentik, A., Waythomas, C.F., 2009. A multidisciplinary effort to assign realistic source parameters to models of volcanic ash-cloud transport and dispersion during eruptions. J. Volcanol. Geotherm. Res. 186, 10–21.

Matoza, R.S., Le Pichon, A., Vergoz, J., Herry, P., Lalande, J.-M., Lee, H.-I., Che, I.-Y., Rybin, A., 2011. Infrasonic observations of the June 2009 Sarychev peak eruption, Kuril islands: implications for infrasonic monitoring of remote explosive volcanism. J. Volcanol. Geotherm. Res. 200, 35–48.

Matoza, R., Fee, D., Neilsen, T.B., Gee, K.L., Ogden, D.E., 2013. Aeroacoustics of volcanic jets: acoustic power estimation and jet velocity dependence. J. Geophys. Res. Solid Earth 118, 6269–6284.

Matoza, R.S., Green, D.N., Le Pichon, A., Shearer, P.M., Fee, D., Mialle, P., Ceranna, L., 2017. Automated detection and cataloging of global explosive volcanism using the international monitoring system infrasound network. Journal of Geophysical Research: Solid Earth 122, 2946–2971.

Matoza, R., Fee, D., Green, D., Mialle, P., 2019. Volcano infrasound and the international monitoring system. Infrasound Monitoring for Atmospheric Studies, pp. 1023–1077.

Mutschlecner, J., Whitaker, R.W., 2010. Some atmospheric effects on infrasound signal amplitudes. Infrasound Monitoring for Atmospheric Studies. Springer, pp. 455–474.

Norris, D., Gibson, R., Bongiovanni, K., 2010. Numerical methods to model infrasonic propagation through realistic specifications of the atmosphere. In: Le Pichon, A., Blanc, E., Hauchecorne, A. (Eds.), Infrasound Monitoring for Atmospheric Studies. Springer Netherlands, Dordrecht, pp. 541–573 https://doi.org/10.1007/978-1-4020-9508-5_17.

Pilger, C., Streicher, F., Ceranna, L., Koch, K., et al., 2013. Application of propagation modeling to verify and discriminate ground-truth infrasound signals at regional distances. InfraMatics 2, 39.

Prata, A. (2020). (personal communication).

Ripepe, M., Bonadonna, C., Folch, A., Delle Donne, D., Lacanna, G., Marchetti, E., Höskuldsson, A., 2013. Ash-plume dynamics and eruption source parameters by infrasound and thermal imagery: the 2010 Eyjafjallajökull eruption. Earth Planet. Sci. Lett. 366, 112–121.

Sparks, R.S.J., Bursik, M.I., Carey, S.N., Gilbert, J., Glaze, L.S., Sigurdsson, H., Woods, A., 1997. Volcanic Plumes. Wiley, Chichester.

Sutherland, L.C., Bass, H.E., 2004. Atmospheric absorption in the atmosphere up to 160 km. J. Acoust. Soc. Am. 115, 1012–1032.

Tailpied, D., Le Pichon, A., Marchetti, E., Ripepe, M., Kallel, M., Ceranna, L., Brachet, N., 2013. Remote infrasound monitoring of Mount Etna: observed and predicted network detection capability. Inframatics 2, 1.

Tailpied, D., Le Pichon, A., Marchetti, E., Assink, J., Vergniolle, S., 2017. Assessing and optimizing the performance of infrasound networks to monitor volcanic eruptions. Geophys. J. Int. 208, 437–448.

Taisne, B., Perttu, A., Tailpied, D., Caudron, C., Simonini, L., 2019. Atmospheric controls on ground- and space-based remote detection of volcanic ash injection into the atmosphere, and link to early warning systems for aviation hazard mitigation. In: Le Pichon, A., Blanc, E., Hauchecorne, A. (Eds.), Infrasound Monitoring for Atmospheric Studies: Challenges in Middle Atmosphere Dynamics and Societal Benefits. Springer International Publishing, Cham, pp. 1079–1105.

Vergniolle, S., Caplan-Auerbach, J., 2006. Basaltic thermals and subplinian plumes: constraints from acoustic measurements at Shishaldin volcano, Alaska. Bull. Volcanol. 68, 611–630.

Waxler, R., Assink, J., 2019. Propagation modeling through realistic atmosphere and benchmarking. In: Le Pichon, A., Blanc, E., Hauchecorne, A. (Eds.), Infrasound Monitoring for Atmospheric Studies: Challenges in Middle Atmosphere Dynamics and Societal Benefits. Springer International Publishing, Cham, pp. 509–549 https://doi.org/10.1007/978-3-319-75140-5_15 URL: doi:10.1007/978-3-319-75140-5_15.

Waxler, R., Assink, J., Velea, D., 2017. Modal expansions for infrasound propagation and their implications for ground-to-ground propagation. The Journal of the Acoustical Society of America 141, 1290–1307.

Whelley, P.L., Newhall, C.G., Bradley, K.E., 2015. The frequency of explosive volcanic eruptions in southeast Asia. Bull. Volcanol. 77 (1).

Whitaker, R.W., Norris, D.E., 2008. Infrasound propagation. In: Havelock, D., Kuwano, S., Vorländer, M. (Eds.), Handbook of Signal Processing in Acoustics. Springer New York, New York, NY, pp. 1497–1519.

Williams, R.A., B, T., Perttu, A., 2020. Processing of volcano infrasound using film sound audio post production techniques to improve signal detection via array processing. Geoscience Letters (7) https://doi.org/10.1186/s40562-020-00158-4.

Woodhouse, M.J., Hogg, A.J., Phillips, J.C., Sparks, R.S.J., 2013. Interaction between volcanic plumes and wind during the 2010 Eyjafjallajökull eruption, Iceland. J. Geophys. Res. Solid Earth 118, 92–109.

Woulff, G., McGetchin, T.R., 1976. Acoustic noise from volcanoes: theory and experiment. Geophys. J. Int. 45, 601–616.

Yamada, T., Aoyama, H., Nishimura, T., Iguchi, M., Hendrasto, M., 2017. Volcanic eruption volume flux estimations from very long period infrasound signals: source estimation with infrasound VLP. Geophys. Res. Lett. 44, 143–151.

Yamada, T., Aoyama, H., Ueda, H., 2018. Relationship between infrasound-derived and buoyancy-derived eruption plume volume estimates. Bull. Volcanol. 80, 71.

Zidikheri, M.J., Lucas, C., Potts, R.J., 2017. Estimation of optimal dispersion model source parameters using satellite detections of volcanic ash: VOLCANIC ASH DISPERSION. J. Geophys. Res. D: Atmos. 122, 8207–8232.